SCIENCE CHINA
Information Sciences

• RESEARCH PAPER •

February 2018, Vol. 61 022201:1–022201:12
https://doi.org/10.1007/s11432-017-9219-1

Parameter influence on electron collection efficiency of a bare electrodynamic tether

Gangqiang LI[1] & Zheng H. ZHU[2*]

[1]*Department of Earth and Space Science and Engineering, York University, Toronto* M3J 1P3*, Canada;*
[2]*Department of Mechanical Engineering, York University, Toronto* M3J 1P3*, Canada*

Received 28 April 2017/Revised 30 May 2017/Accepted 5 July 2017/Published online 22 December 2017

Abstract This study develops a coupled multiphysics finite element method for the dynamic analysis of a bare flexible electrodynamic tether. Contrary to the existing methods, the new method discretizes and solves the orbital motion limited equation and the dynamic equation of an elastic flexible tether simultaneously. First, the new method is verified via comparison with the existing methods in a straight tether situation. Second, the number of tether elements, tether bending deformation, and two design parameters at the cathodic end affecting the electrical current are investigated. It is determined that the tether bending deformation and the two parameters i.e., the impedance Z_T and Φ_{PW} have a significant impact on the electron collection efficiency of an electrodynamic tether system. The results indicate that the proposed method should be applied in the refined mission analysis.

Keywords multiphysics, coupled, finite element, electrodynamic tether, electron collection efficiency

Citation Li G Q, Zhu Z H. Parameter influence on electron collection efficiency of a bare electrodynamic tether. Sci China Inf Sci, 2018, 61(2): 022201, https://doi.org/10.1007/s11432-017-9219-1

1 Introduction

The ever-increasing population of space debris poses a significant threat to the on-orbit serving spacecraft; thus, it has been a growing concern for the academic and industrial communities [1]. Many novel space debris capturing and removal methods have been proposed and developed [2]. Among these, the electrodynamic tether (EDT) system is an appealing technology as an active space debris removal system owing to its advantages of low mass, compact size, lack of propellant, and ease of operation [3, 4]. Over the past few decades, significant efforts have been devoted to the study of dynamics and the analysis of stability of a rigid/flexible EDT system [3], and many control strategies based on different kinds of mechanisms have been proposed to stabilize the EDT system [5–10]. Among them, the electrical current regulation strategy is a simple implementation method [5, 6, 8, 9]. Therefore, the understanding and evaluation of the induced current of the EDT system with high accuracy is an important issue. However, in reality, the conductive tether experiences a bending deformation in the deorbit process owing to perturbative forces [11, 12]. Therefore, a high accuracy calculation method with consideration of the realistic tether geometry is necessary.

Electron collection occurs in the orbital motional limited (OML) regime if the effective diameter of the tape tether is smaller than the Debye length [13, 14]. Moreover, the generation of electrical current is constrained by the boundary conditions at each end, and it is a two-point boundary value problem as

* Corresponding author (email: gzhu@yorku.ca)

presented in [13, 15]. Many approaches based on the rigid or flexible tether model have been proposed and developed [9, 13, 14, 16–18]. For instance, the optimization methods have generally been applied to solve the non-dimensional OML equations of the rigid tether model [13]. Subsequently, the flexible tether model of the EDT system was developed; however, the empirical formulas [19] and the OML equations based on the rigid tether model are still used [7, 9, 18]. The dynamic equations of the flexible tether model and OML equations are roughly combined together. The electrical current is calculated independently in a straight and vertical tether situation; subsequently, it is manually projected onto the tether, which may be bent. As presented in [12, 15], the electrical current is dependent not only on the environment parameters, such as the magnetic field strength and electron density of ionospheric plasmas, but also on the tether parameters, such as the width, thickness, and electromotive force (EMF) E_m of the tether. It was determined that the existing approaches for the evaluation of induced current are mainly based on the following assumptions: (i) the effective diameter of the tether is assumed to be smaller than the Debye length [13]; (ii) the conductive tether is a straight and rigid tether, and it always aligns in the local vertical direction [13]; (iii) the EMF E_m is constant along the whole tether and its value is calculated at the center of mass of the EDT system [13, 20]; (iv) the boundary condition at the cathodic end is simplified [15]; (v) the OML theory and tether dynamics are not fully coupled and simultaneously solved [17, 18]. Many efforts have been made to address the aforementioned assumptions. For instance, the G function is introduced to consider the beyond OML effect caused by a wide tape tether [15]. The results demonstrate that the beyond OML effect should be considered in the refined mission analysis. The ad-hoc method of the OML theory is proposed, where a scaling factor $\alpha = L'/L$ is introduced to consider the bending effect of the tether affecting the electron collection efficiency, and the modified electromotive force is expressed as $E_m = \alpha \cdot E_m$. This method has been successfully incorporated into the flexible tether model to predict the dynamic response of the EDT system in the deorbit process [17]. Furthermore, the ad-hoc method is unable to differentiate different bending profiles of tether with the same end nodes, for example, the difference between the semicircle and the S-shape profiles with the same end nodes [11, 12]. It indicates that the variation of electron collection efficiency along the tether cannot be considered. Accordingly, a finite element method is introduced to consider the coupling effect between the tether deflection and electrodynamic force [11, 12]. The results show that this method is effective to capture the coupling effect between the tether deflection and the electrodynamic force. However, this method has two drawbacks: (i) the computation load is high owing to the calculation of the non-dimensional element length by using the Gaussian integration [12]; (ii) the mathematical stability of this approach is poor when the tether experiences a large bending motion. The non-dimensional OML equation is solved in a piecewise manner and the values of electrical current and potential bias at the common nodes of adjacent elements may be different and require manual adjustment. Subsequently, sets of parameters α_i and β_i $(i = 1, \ldots, n)$ are introduced to enforce the continuity of the electrical current and potential bias when the tether experiences a large bending motion. The poor numerical stability is attributed to the significant changes of these scaling parameters [12]. In order to address these two drawbacks, a new discretization method is proposed based on the dimensional OML equation [21], wherein both the Gaussian integration process and the parameters α_i and β_i $(i = 1, \ldots, n)$ are cancelled out. In this approach, a two-loop procedure exists—the first loop is intended for the fixed-point iteration of the tether dynamics, and the second loop is intended for the Newton-Raphson iteration of the OML theory [21]. Furthermore, the tether dynamic equations and discretized OML equations are not simultaneously solved. In addition, the sensitivity analysis of the parameter of the configuration of electric circuit at the cathodic end is not performed [21]. Therefore, a fully coupled model between the tether dynamics and the OML theory with good mathematical stability is desired, and they should be solved simultaneously.

In this study, a fully coupled multiphysics finite element method is developed to solve the OML theory and tether dynamics simultaneously. In this approach, the tether is spatially divided into a series of finite elements, and the dynamics of the flexible tethers and OML equations are discretized by using the same mesh. The nodal position, potential bias, and electrical current are the state variables, and they are simultaneously solved by using a symplectic algorithm.

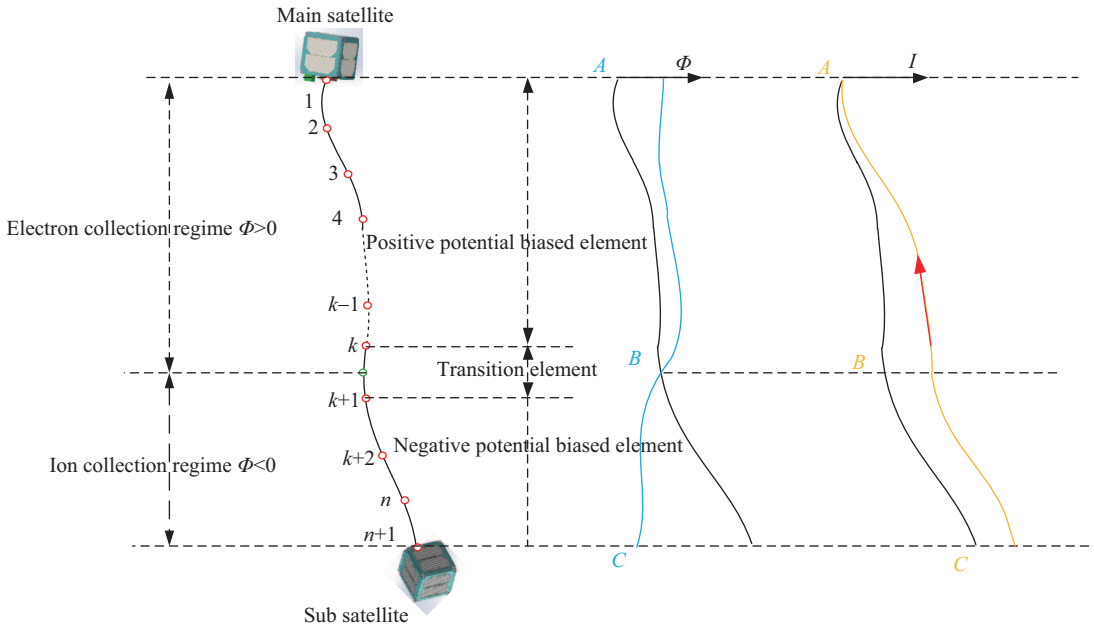

Figure 1 (Color online) Profiles of electrical current and potential bias along a bent tether.

2 Multiphysics formulation of flexible electrodynamic tether satellite system

Consider the flexible EDT system shown in Figure 1. It consists of a conductive bare tape-type tether, and a main and sub-satellite. It is assumed that the main satellite deploys the tether and sub-satellite downwards. A field emitter array is used as a cathode to expel electrons into the ambient plasma to complete the electric circuit [8, 22]. The emitter is installed on the main satellite and sub-satellite in order to improve the efficiency of the EDT system in highly inclined orbits, where the electrical polarity reverses in one orbit [19, 22]. The tether is spatially discretized by the nodal position finite element method, where the nodal positions, as opposed to the displacements in the conventional finite element method, are used as state variables. The governing equation of motion of tether dynamics is derived from the principle of virtual work [23, 24]. Considering the kth element as an example, it can be expressed as

$$\boldsymbol{M}\ddot{\boldsymbol{X}}_{\mathrm{e}} + \boldsymbol{K}\boldsymbol{X}_{\mathrm{e}} = \boldsymbol{F}_{\mathrm{e}}^{k0} + \boldsymbol{F}_{\mathrm{e}}^{g} + \boldsymbol{F}_{\mathrm{e}}^{d} + \boldsymbol{F}_{\mathrm{e}}^{sp} + \boldsymbol{F}_{\mathrm{e}}^{l}, \tag{1}$$

where $\boldsymbol{X}_{\mathrm{e}}$ and $\ddot{\boldsymbol{X}}_{\mathrm{e}}$ are the position and acceleration vectors of the element [20, 24]; $\boldsymbol{M}$ and $\boldsymbol{K}$ are the mass and stiffness matrices of the tether element; $\boldsymbol{F}_{\mathrm{e}}^{k0}\boldsymbol{F}_{\mathrm{e}}^{g}$, $\boldsymbol{F}_{\mathrm{e}}^{d}$, $\boldsymbol{F}_{\mathrm{e}}^{sp}$, and $\boldsymbol{F}_{\mathrm{e}}^{l}$ are the force terms of the element resulting from the stiffness of the tether, gravity, atmosphere drag, solar pressure, and electrodynamic force, respectively. Here, the subscript "e" stands for element. All these orbital perturbation forces, except for the electrodynamic force $\boldsymbol{F}_{\mathrm{e}}^{l}$, can be found in [9, 20]. Notably, the internal damping is not incorporated here owing to the lack of experimental data in space. Nonetheless, the damping effect generally stabilizes the dynamics of the tether system and thus, neglecting the damping will not affect the validity of the current investigation. The final dynamic equation of the tethered satellite system can be obtained by using the standard assembly procedure in the conventional finite element. The electrodynamic force $\boldsymbol{F}_{\mathrm{e}}^{l}$ depends on the electrical current in the tether, which will be determined in the following subsection.

The electrodynamic force $\boldsymbol{F}_{\mathrm{e}}^{l}$ exerting on the tether element in (1) results from the interaction between the current carrying tether and the earth's magnetic field. In the current study, the equivalent diameter of the tape-type tether is less than the Debye length; hence, the current-potential bias relationship ($I-\Phi$ of a bare EDT system obeys the OML theory [25]. The governing equations of electrical current I and

potential bias Φ can be expressed as

$$\begin{cases} \dfrac{\mathrm{d}I}{\mathrm{d}x} = a_1 a_2 \sqrt{\Phi}, \\ \dfrac{\mathrm{d}\Phi}{\mathrm{d}x} = a_3 I - E_m, \end{cases} \qquad \Phi > 0, \tag{2}$$

$$\begin{cases} \dfrac{\mathrm{d}I}{\mathrm{d}x} = -\mu a_1 a_2 \sqrt{(-\Phi)}, \\ \dfrac{\mathrm{d}\Phi}{\mathrm{d}x} = a_3 I - E_m, \end{cases} \qquad \Phi < 0, \tag{3}$$

where $a_1 = qp_tN_\mathrm{e}/\pi$, $a_2 = \sqrt{2q/m_\mathrm{e}}$, and $a_3 = 1/\sigma A_t$ are the parameters of the tether, $p_t = 2\,(w+t)$ is the perimeter of tape tether, q is the elementary charge, N_e is the density of electron. Further, E_m is the EMF. Notably, the parameters a_1 and E_m are not constant, and they vary significantly along the tether when the tether experiences a large bending motion [12, 19].

Moreover, the boundary conditions at the anodic and cathodic ends and the position of null potential bias point inside the tether are defined as

$$\begin{aligned} &x = 0, \quad I = 0, \quad \Phi = \Phi_A, \\ &x = L_B, \quad I = I_B, \quad \Phi = \Phi_B = 0, \\ &x = L_C, \quad I = I_C, \quad \Phi = \Phi_C, \end{aligned} \tag{4}$$

where L_B is the unknown length of the positively biased segment, and it should be updated at each iteration step.

There are two design configurations of the field emitter electric circuit at the cathodic end as shown in Figure 2. In the first case, an additional battery is required to neutralize the potential bias of point C in order to maximize the electron collection efficiency of the EDT system [12]. In the second case, the tether directly connects to the base of the field emitter. The mathematical expressions can be obtained as

$$\Phi_C = |\Phi_\mathrm{PW}| - |\Phi_\mathrm{CHE}| + I_C Z_T, \tag{5}$$

$$\Phi_C = -|\Phi_\mathrm{CHE}| + I_C Z_T, \tag{6}$$

where Z_T is the equivalent impedance of the emitter electric circuit, which is determined by an experimental test, Φ_CHE is the potential bias of the battery of the emitter, and Φ_PW is the potential bias of the additional battery.

In the current study, Eqs. (2) and (3) are directly discretized in space by using the same shape function in the tether dynamics [20, 24]. Altogether, three types of elements are defined according to the variation characteristic of the potential bias along the element length. They are categorized as the positively biased element ($\Phi > 0$), the negatively biased element ($\Phi < 0$), and the transition element where the null potential point resides and the potential bias inside the element is partially positive and partially negative. As shown in Figure 1, the tether is divided into n elements with $n+1$ nodes, and the null potential bias point is temporarily assumed to be located inside the kth element.

First, regarding the positively biased element located inside the electron collection regime, e.g., the jth elements ($j < k$), the discretized OML equations are expressed as (7). Second, regarding the negatively biased element located inside the ion collection regime, e.g., the jth elements ($j > k$), the discretized OML equations are expressed as (8). Finally, for the transitional element, i.e., the kth element, the discretized OML equations are expressed as (9).

$$\begin{bmatrix} -\dfrac{1}{L_j} & -\dfrac{a_{1,j}a_{2,j}}{\sqrt{\Phi_j}} & \dfrac{1}{L_j} & 0 \\ -a_{3,j} & -\dfrac{1}{L_j} & 0 & \dfrac{1}{L_j} \end{bmatrix} \cdot \begin{Bmatrix} I_j \\ \Phi_j \\ I_{j+1} \\ \Phi_{j+1} \end{Bmatrix} = \begin{Bmatrix} 0 \\ -E_m^j \end{Bmatrix}, \quad j = (0, 1, \ldots, k-1), \tag{7}$$

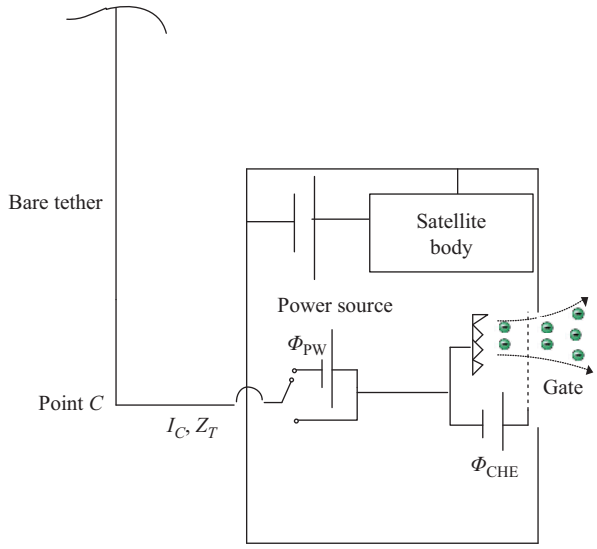

Figure 2 (Color online) Design schematic of electrical circuit at the cathodic end.

$$\begin{bmatrix} -\dfrac{1}{L_j} & -\dfrac{\mu a_{1,j}a_{2,j}}{\sqrt{(-\Phi_j)}} & \dfrac{1}{L_j} & 0 \\ -a_{3,j} & -\dfrac{1}{L_j} & 0 & \dfrac{1}{L_j} \end{bmatrix} \cdot \begin{Bmatrix} I_j \\ \Phi_j \\ I_{j+1} \\ \Phi_{j+1} \end{Bmatrix} = \begin{Bmatrix} 0 \\ -E_m^j \end{Bmatrix}, \quad j = (k+1, k+2, \ldots, n+1), \tag{8}$$

where L_j is the instantaneous length of jth element, E_m^j is the EMF of jth element, and $a_{1,j}$, $a_{2,j}$, and $a_{3,j}$ are the tether parameters as defined in (2) with the subscript denoting the jth element.

$$\begin{bmatrix} b_{11} & b_{12} & \dfrac{1}{L_k^{\mathrm{N}}} & 0 \\ -a_{3,k}\dfrac{L_k}{L_k^{\mathrm{N}}} & \dfrac{-a_{1,k}a_{2,k}a_{3,k}L_k^{\mathrm{P}}}{\sqrt{\Phi_k}} - \dfrac{1}{L_k^{\mathrm{N}}} & 0 & \dfrac{1}{L_k^{\mathrm{N}}} \end{bmatrix} \cdot \begin{Bmatrix} I_k \\ \Phi_k \\ I_{k+1} \\ \Phi_{k+1} \end{Bmatrix} = \begin{Bmatrix} \dfrac{-\mu a_{1,k}a_{2,k}L_k^{\mathrm{P}}}{\sqrt{-\left(\Phi_k - E_m^k L_k^{\mathrm{P}} + a_{3,k}I_k L_k^{\mathrm{P}}\right)}} E_m^k \\ -\dfrac{L_k}{L_k^{\mathrm{N}}} E_m^k \end{Bmatrix}, \tag{9}$$

where L_k^{P} and L_k^{N} are the unknown lengths of the positive and negative segments of the transition element. They can be initially approximated as $L_k^{\mathrm{P}} = |\Phi_k|\, L_k/(|\Phi_k| + |\Phi_{k+1}|)$ and $L_k^{\mathrm{N}} = L_k - L_k^{\mathrm{P}}$, where L_k is the instantaneous length of the kth element, and it should be updated by using the same technique at each iteration step. The element entries b_{11} and b_{12} in (10) are expressed as

$$\begin{aligned} b_{11} &= -\frac{1}{L_k^{\mathrm{N}}} - \frac{\mu a_{1,k}a_{2,k}a_{3,k}L_k^{\mathrm{P}}}{\sqrt{-\left(\Phi_k - E_m^k L_k^{\mathrm{P}} + a_{3,k}I_k L_k^{\mathrm{P}}\right)}}, \\ b_{12} &= -a_{1,k}a_{2,k}\left[\frac{L_k^{\mathrm{P}}}{L_k^{\mathrm{N}}\sqrt{\Phi_k}} + \frac{\mu}{\sqrt{-\left(\Phi_k - E_m^k L_k^{\mathrm{P}} + a_{3,k}I_k L_k^{\mathrm{P}}\right)}}\right]. \end{aligned} \tag{10}$$

There are $2(n+1)$ unknown variables of the potential bias and electrical current for the discretized n elements; however, there are $2n$ algebraic nonlinear equations and two additional algebraic equations are required to obtain the true solution. These two algebraic equations can be obtained through the discretization of the boundary conditions at the anodic and cathodic ends, and they are expressed as

$$\left\{\, 1 \;\; 0 \;\; 0 \;\; 0 \,\right\} \cdot \left\{\, I_1 \;\; \Phi_1 \;\; I_2 \;\; \Phi_2 \,\right\}^{\mathrm{T}} = 0, \tag{11}$$

$$\left\{\, 0 \;\; 0 \;\; -Z_T \;\; 1 \,\right\} \cdot \left\{\, I_n \;\; \Phi_n \;\; I_{n+1} \;\; \Phi_{n+1} \,\right\} = \begin{cases} |\Phi_{\mathrm{PW}}| - |\Phi_{\mathrm{CHE}}|\,, \\ -|\Phi_{\mathrm{CHE}}|\,. \end{cases} \tag{12}$$

Thus, the final discretized OML equations of a bare EDT system can be obtained by assembling (7)–(12) by using the same assembly procedure as in the nodal position finite element. The finalized OML equations can be expressed as

$$\boldsymbol{K}' \cdot \boldsymbol{Z} = \boldsymbol{F}' \tag{13}$$

where $\boldsymbol{K}'$ is the global coefficient matrix with dimensions $(2n+2, 2n+2)$. Notably, it does not explicitly contain the position vector $\boldsymbol{X} = (X_1, Y_1, Z_1, \ldots, X_{n+1}, Y_{n+1}, Z_{n+1})^{\mathrm{T}}$. Further, $\boldsymbol{Z} = \{I_1, \Phi_1, \ldots, I_{n+1}, \Phi_{n+1}\}^{\mathrm{T}}$ is the column vector of the unknown electrical current and potential bias and $\boldsymbol{F}'$ is a $2n+2$ dimensional column vector.

When the discretized equation (13) is numerically solved, and the profiles of electrical current and potential bias along the flexible tether are obtained, the exerting electrodynamic force $\boldsymbol{F}_{\mathrm{e}}^{l}$ listed in (14) can be evaluated as

$$\boldsymbol{F}_{\mathrm{e}}^{l} = \int_0^{L_{\mathrm{e}}} \boldsymbol{N}^{\mathrm{T}} \boldsymbol{f}_{\mathrm{g}}^{l} \mathrm{d}s = \frac{L_{\mathrm{e}}}{2} \sum_{t=1}^{20} w_t \boldsymbol{N}^{\mathrm{T}} \left[\frac{L_{\mathrm{e}}}{2}(1+\kappa_t) \right] \boldsymbol{f}_{\mathrm{g}}^{l} \left[\frac{L_{\mathrm{e}}}{2}(1+\kappa_t) \right], \tag{14}$$

where $\boldsymbol{f}_{\mathrm{g}}^{l} = \boldsymbol{T}_{l2\mathrm{g}} \boldsymbol{f}_{l}^{l}$ and $\boldsymbol{f}_{l}^{l} = (-\boldsymbol{B}_l \times I\boldsymbol{t}^{\mathrm{e}})$ are the electrodynamic force vectors per unit length in the global and local tether frames, respectively, $\boldsymbol{T}_{l2\mathrm{g}}$ is the transpose matrix of the transformation matrix $\boldsymbol{T}_{\mathrm{g}2l}$ presented above, (w_t, κ_t) are the weight and abscissa of the Gaussian integral, respectively, and $\boldsymbol{N}^{\mathrm{T}}$ is the shape function matrix of a two-node tether element as defined in [23, 24, 26].

In the current study, the set of $2n+2$ nonlinear algebraic equations (13) can be treated as a set of constraint equations of the tether dynamic equation, and the coupling model of the OML theory and the tether dynamics can be obtained by combining (1) and (13) together such that

$$\begin{cases} \boldsymbol{M}\ddot{\boldsymbol{X}} + \boldsymbol{K}\boldsymbol{X} = \boldsymbol{F}^{\mathrm{ext}}(t, \boldsymbol{X}, \boldsymbol{Z}), \\ \boldsymbol{K}'(\boldsymbol{X})\boldsymbol{Z} = \boldsymbol{F}', \end{cases} \tag{15}$$

where $\boldsymbol{F}^{\mathrm{ext}}$ is the superposition of all the external forces as listed in (1).

As presented in [11, 22], the deorbiting process of a defunct satellite by using bare EDT equipment is a long-term process. Consequently, a desirable numerical integration algorithm for the deorbit process should have long-time stability and preserve the global geometric structure in the phase space. Further, the Symplectic integrator preserves a Symplectic transformation at every point of the phase space. Moreover, it imposes a stringent condition on the global geometry of the dynamics. Thus, the Symplectic integration algorithm should be normally applied for the deorbiting process of a defunct satellite. In the present study, the implicit middle point scheme is employed, and it can be expressed as

$$\boldsymbol{X}_{n+1} - \boldsymbol{X}_n = \frac{\Delta t_{n+1}}{2}(\dot{\boldsymbol{X}}_{n+1} + \dot{\boldsymbol{X}}_n), \tag{16}$$

$$\dot{\boldsymbol{X}}_{n+1} - \dot{\boldsymbol{X}}_n = \frac{\Delta t_{n+1}}{2}(\ddot{\boldsymbol{X}}_{n+1} + \ddot{\boldsymbol{X}}_n), \tag{17}$$

where $\boldsymbol{X}$, $\dot{\boldsymbol{X}}$, and $\ddot{\boldsymbol{X}}$ are the vectors of nodal position, velocity, and acceleration of discretized EDT systems, respectively, with the subscripts $n+1$ and n representing the variables in the current and previous steps, respectively. Further, $\Delta t_{n+1} = t_{n+1} - t_n$ is the time step-size at the current time.

Finally, Eqs. (15)–(17) can be combined together, and a series of algebraic nonlinear equations are obtained as follows:

$$\boldsymbol{G} = \begin{pmatrix} \boldsymbol{G}_1 \\ \boldsymbol{G}_2 \\ \boldsymbol{G}_3 \\ \boldsymbol{G}_4 \end{pmatrix} = \begin{pmatrix} \boldsymbol{M}_{n+1}\ddot{\boldsymbol{X}}_{n+1} + \boldsymbol{K}_{n+1}\boldsymbol{X}_{n+1} - \boldsymbol{F}_{n+1}^{\mathrm{ext}} \\ 2\boldsymbol{X}_{n+1} - \Delta t_{n+1}\dot{\boldsymbol{X}}_{n+1} - 2\boldsymbol{X}_n - \Delta t_{n+1}\dot{\boldsymbol{X}}_n \\ 2\dot{\boldsymbol{X}}_{n+1} - \Delta t_{n+1}\ddot{\boldsymbol{X}}_{n+1} - 2\dot{\boldsymbol{X}}_n - \Delta t_{n+1}\ddot{\boldsymbol{X}}_n \\ \boldsymbol{K}'_{n+1} \cdot \boldsymbol{Z}_{n+1} - \boldsymbol{F}'_{n+1} \end{pmatrix} = \boldsymbol{0}. \tag{18}$$

In total, the system has $5(n+1)$ unknowns including $3(n+1)$ position related unknows and $2(n+1)$ potential related unknowns. The former includes vectors of acceleration $\ddot{\boldsymbol{X}}_{n+1}$, velocity $\dot{\boldsymbol{X}}_{n+1}$, and

Table 1 Physical parameters of EDT system

Parameter	Value
Tether material	Aluminum
Elastic modulus of tether ($\mathrm{N}\cdot\mathrm{m}^{-2}$)	7.2×10^{10}
Density of tether material ($\mathrm{kg/m}^3$)	2700
Tether length (m)	500
Tether width (m)	0.004
Tether thickness (μm)	35
Mass of main satellite (kg)	2
Mass of sub-satellite (kg)	2
Dimensions of main satellite (m)	$0.1\times0.1\times0.1$
Dimensions of sub-satellite (m)	$0.1\times0.1\times0.1$

position $\boldsymbol{X}_{n+1}$, while the latter includes the vector of potential $\boldsymbol{Z}_{n+1}$. Notably, the number of nonlinear algebraic equations is equal to the number of unknown variables. Therefore, in principle, a unique solution of the coupling equation of the tether dynamics and OML theory can be obtained. In the current study, the iterative Newton-Raphson method is employed, which can be expressed as

$$\begin{bmatrix} \frac{\partial \boldsymbol{G}_1}{\partial \ddot{\boldsymbol{X}}_{n+1}} & \frac{\partial \boldsymbol{G}_1}{\partial \dot{\boldsymbol{X}}_{n+1}} & \frac{\partial \boldsymbol{G}_1}{\partial \boldsymbol{X}_{n+1}} & \boldsymbol{0} \\ \frac{\partial \boldsymbol{G}_2}{\partial \ddot{\boldsymbol{X}}_{n+1}} & \frac{\partial \boldsymbol{G}_2}{\partial \dot{\boldsymbol{X}}_{n+1}} & \frac{\partial \boldsymbol{G}_2}{\partial \boldsymbol{X}_{n+1}} & \boldsymbol{0} \\ \frac{\partial \boldsymbol{G}_3}{\partial \ddot{\boldsymbol{X}}_{n+1}} & \frac{\partial \boldsymbol{G}_3}{\partial \dot{\boldsymbol{X}}_{n+1}} & \frac{\partial \boldsymbol{G}_3}{\partial \boldsymbol{X}_{n+1}} & \boldsymbol{0} \\ \boldsymbol{0} & \boldsymbol{0} & \boldsymbol{0} & \frac{\partial \boldsymbol{G}_4}{\partial \boldsymbol{Z}_{n+1}} \end{bmatrix}^m \cdot \begin{Bmatrix} \Delta\ddot{\boldsymbol{X}}_{n+1} \\ \Delta\dot{\boldsymbol{X}}_{n+1} \\ \Delta\boldsymbol{X}_{n+1} \\ \Delta\boldsymbol{Z}_{n+1} \end{Bmatrix}^m = \begin{Bmatrix} \boldsymbol{G}_1 \\ \boldsymbol{G}_2 \\ \boldsymbol{G}_3 \\ \boldsymbol{G}_4 \end{Bmatrix}^m, \tag{19}$$

where Δ indicates the Newton difference, the superscript m denotes the mth iteration, and $\boldsymbol{G}_1$, $\boldsymbol{G}_2$, $\boldsymbol{G}_3$, and $\boldsymbol{G}_4$ are defined as

$$\begin{cases} \boldsymbol{G}_1 = \boldsymbol{M}_{n+1}\ddot{\boldsymbol{X}}_{n+1} + \boldsymbol{K}_{n+1}\boldsymbol{X}_{n+1} - \boldsymbol{F}^{\mathrm{ext}}_{n+1}, \\ \boldsymbol{G}_2 = 2\boldsymbol{X}_{n+1} - \Delta t_{n+1}\dot{\boldsymbol{X}}_{n+1} - 2\boldsymbol{X}_n - \Delta t_{n+1}\dot{\boldsymbol{X}}_n, \\ \boldsymbol{G}_3 = 2\dot{\boldsymbol{X}}_{n+1} - \Delta t_{n+1}\ddot{\boldsymbol{X}}_{n+1} - 2\dot{\boldsymbol{X}}_n - \Delta t_{n+1}\ddot{\boldsymbol{X}}_n, \\ \boldsymbol{G}_4 = \boldsymbol{K}'_{n+1}\cdot\boldsymbol{Z}_{n+1} - \boldsymbol{F}'_{n+1}. \end{cases} \tag{20}$$

Notably, the element entries of the Jacobian matrix are calculated using the numerical differentiation, except $\partial\boldsymbol{G}_4/\partial\mathbf{Z}_{n+1}$, which can be obtained in an analytical form. Moreover, the explicit forward Euler method is applied to generate the initial iteration values of the vectors of velocity $\dot{\boldsymbol{X}}_{n+1}$ and acceleration $\ddot{\boldsymbol{X}}_{n+1}$. The accuracy of this iteration solver is controlled by a set of parameters called the tolerance $\varepsilon = \sum_{i=1}^{4}|\boldsymbol{G}_i|/(5n+5) \leqslant 10^{-10}$ and the maximum iteration number $m = 50$.

3 Simulation results and discussion

The newly developed coupled multiphysics finite element method is applied to investigate the variation of system parameters affecting the results of electrical current and potential bias of a bare flexible EDT system. First, the new approach is compared with the existing solutions based on the continuous electrical current profile solved by the reference method in [12, 17]. The physical parameters of the EDT system used in the current study are given in Table 1, which are based on the demonstration mission of space debris removal by the EDT system [27].

3.1 Benchmark study

In this subsection, the proposed method is compared with two reference methods — the first method is based on the non-dimensional OML equations [12], and the second reference method is a discretization method of the dimensional OML equation [21]. Notably, the only difference between the current approach

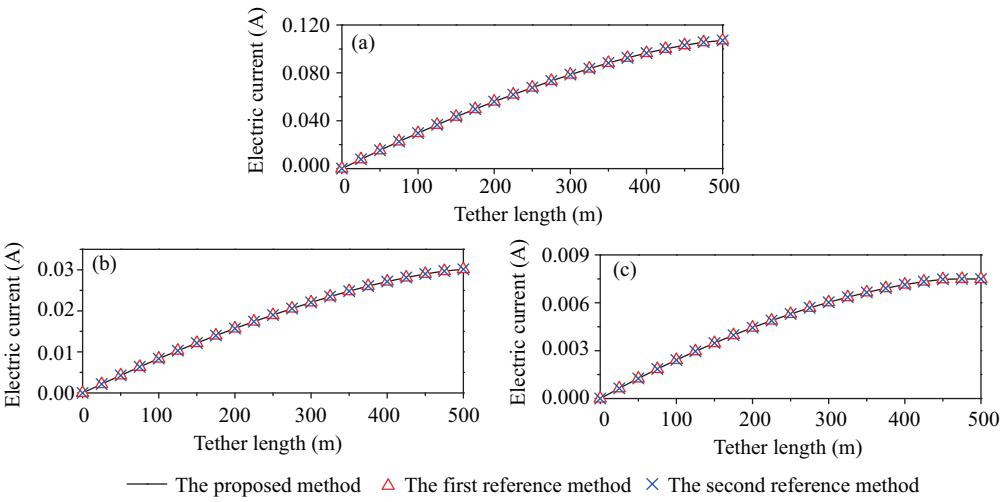

Figure 3 (Color online) Comparisons of current profiles along a straight tether in different orbits with different calculation methods. (a) Equatorial orbit; (b) 53° inclined orbit; (c) Polar orbit.

Table 2 Maximum current at the anodic end (A)

Name	The first reference method	The second reference method	The proposed method
Equatorial orbit	0.1070854	0.1070634	0.1070633
53° inclined orbit	0.0301559	0.0301567	0.0301569
Polar orbit	0.0074935	0.0074924	0.0074921

Table 3 Length of positively biased segment in different cases (m)

Name	The first reference method	The second reference method	The proposed method
Equatorial orbit	497.5217	497.5222	497.5222
53° inclined orbit	498.5358	498.5365	498.5365
Polar orbit	482.3310	482.3293	482.3293

and the reference method is the combination procedure between the electrical current generation module and the tether dynamic module. In order to maintain the accuracy of these comparison methods at a similar level and ensure that they are comparable, the integration method of the reference method [12, 21] is changed to the middle point Symplectic method. The tether is assumed to align with the local vertical with the main satellite on the top, and the initial altitude is assumed to be 450 km. In this subsection, the values of Z_T, $\Phi_{\rm CHE}$, and $\Phi_{\rm PW}$ at the cathodic end are set as 5 Ω, 50 V, and 50 V, respectively. The numerical simulations are carried out in three orbits, i.e., the equatorial orbit, 53° inclined orbit, and polar orbit. The 53° inclined orbit is chosen as the orbit of the demonstration mission of the EDT technology. In this section, the tether is discretized into 20 elements as shown in the convergence study, which will be presented in next subsection.

The comparison results are shown in Figure 3 and Tables 2 and 3, where Figure 3 shows the comparison results of the profiles of electrical current along a straight conductive tether in different orbits. It can be observed that the results of the proposed method are consistent with the results of these two reference methods. The difference between these two methods derived from the dimensional OML theory can be ignored in a vertical straight case. As explained in the previous section, the only difference is the combination procedure between the tether dynamic equations and the discretized OML equations. Regarding the second reference method [21], a two-loop procedure exists at each time step — the first loop is the fixed-point iteration for the tether dynamics, and the second loop is the Newton-Raphson iteration for the discretized OML equations. However, in the proposed method, there is only one-loop procedure for the fixed-point iteration of (18). Moreover, the comparison results of the maximum current I_B and the length of positive bias segment L_B demonstrate that the difference between these comparison methods can be ignored in a straight tether case, as listed in Tables 2 and 3. However, the integration

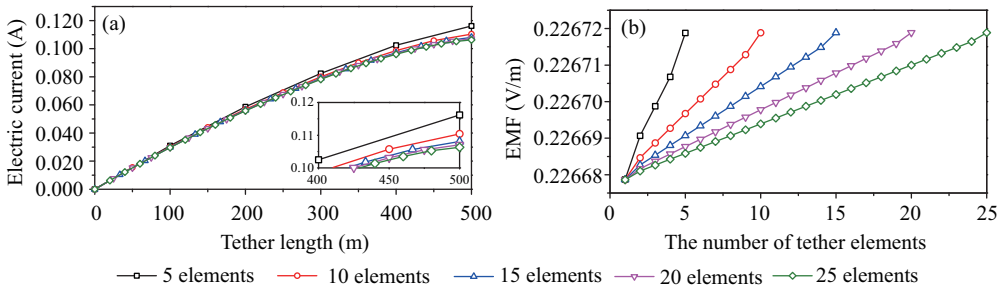

Figure 4 (Color online) Analysis of the number of tether elements. (a) Electrical current profile along tether; (b) EMF profile along tether.

Table 4 Maximum current and potential bias

Name	5 elements	10 elements	15 elements	20 elements	25 elements
Current I_B (A)	0.116	0.110	0.108	0.107	0.106
Potential bias Φ_A (V)	109.991	109.818	109.777	109.753	109.744

process for the calculation of length of the non-dimensional element is avoided [12], which saves the time computational efforts.

3.2 Parameter analysis

In this subsection, the number of tether elements, tether bending effect, value of additional battery potential bias $\Phi_{\rm PW}$, and equivalent impedance Z_T of the cathodic electric circuit affecting the profiles of electrical current are thoroughly investigated. The initial altitude is set as 450 km with a circular equatorial orbit. The potential bias of emitter $\Phi_{\rm CHE}$ is fixed at 50 V according to the characteristic of field emitter array [9].

First, the number of tether elements affecting the accuracy of the induced electrical current is investigated in a straight tether situation. The potential bias of the additional battery $\Phi_{\rm PW}$ and impedance Z_T at the cathodic end are set as 50 V and 5 Ω, respectively. The results are shown in Figure 4 and Table 4. As evident in Figure 4, a larger number of elements leads to a better approximation of the profile of EMF along the tether, and consequently, higher accuracy of the results. The same conclusion can be obtained from the results of the variation of maximum current I_B and potential bias Φ_A, as listed in Table 4. For instance, the accuracy of the electrical current I_B increases as the number of tether elements increases. However, the difference between the length of positive potential bias segment L_B of 20 elements and 25 elements is smaller than that of 15 elements and 20 elements. However, the computational loads will be significantly increased if the tether is divided into 25 elements. Thus, the tether is divided into 20 elements in the following sections after the tradeoff between the accuracy and computational loads.

Second, a parameter γ is defined to investigate the bending effect of tether geometry in [12, 21]. In this subsection, the bending effect is investigated by varying γ from 0.04 to 0.32 as shown in Figure 5(a), and nine cases are analyzed. The values of $\Phi_{\rm PW}$ and Z_T at the cathodic end are set the same as in the previous case. The results are shown in Figure 5(c)–(d). Further, the EMF, electrical current, and potential bias change significantly as the tether bends more. This significant change of EMF of a bent tether indicates the assumption of constant EMF along the tether length is not reasonable [13, 20]. Moreover, the results show that the tether geometry profile significantly affects the electron collection efficiency of an EDT system [12]. For instance, the current I_C at the cathodic end decreases from 0.105 to 0.080 as shown in Figure 5(c). The same phenomenon can also be observed in the results of the length of positive potential bias L_B as listed in Table 5, as it decreases from 497.53 m to 471.55 m. Consequently, the effect of tether bending deformation must be considered in the evaluation of the electrical current.

Third, the value of impedance Z_T and the potential bias of additional battery $\Phi_{\rm PW}$ at the cathodic end affecting the electrical current are investigated. The tether is assumed to be straight and aligned with the local vertical, and the initial altitude is 450 km in a circular equatorial orbit. Further, Z_T varies

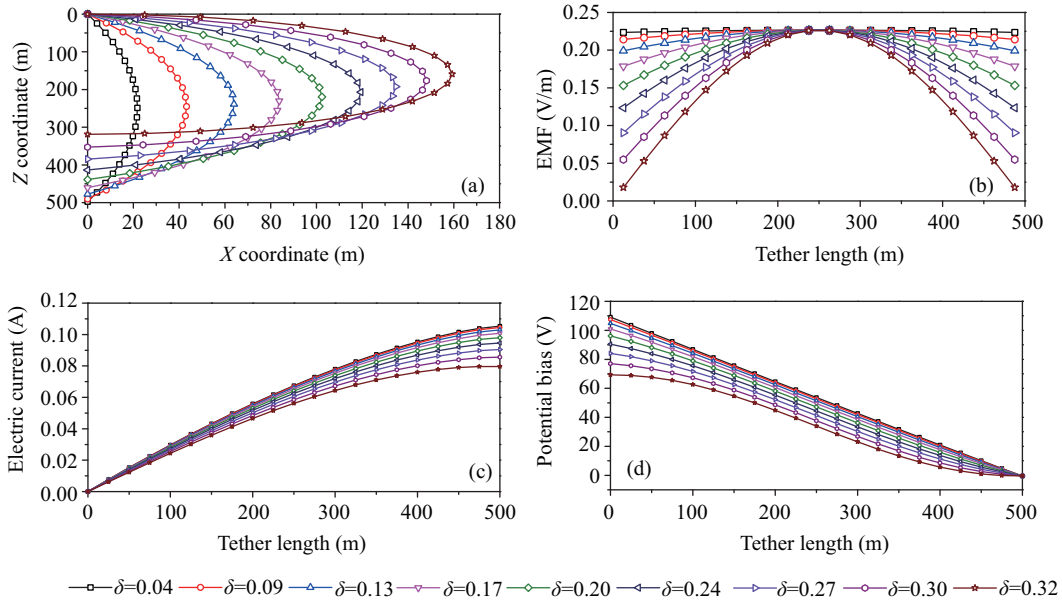

Figure 5 (Color online) Analysis of the tether bending effect. (a) Tether profile; (b) EMF profile along tether; (c) electrical current profile along tether; (d) potential bias profile along tether.

Table 5 The length L_B in different cases

Name	$\delta = 0.04$	$\delta = 0.09$	$\delta = 0.13$	$\delta = 0.17$	$\delta = 0.20$	$\delta = 0.24$	$\delta = 0.27$	$\delta = 0.30$	$\delta = 0.32$
Length L_B (m)	497.53	497.44	497.28	497.01	496.58	495.85	494.44	490.74	471.55

Table 6 Length L_B and maximum current I_A in different cases

	Z_T=5 Ω	Z_T=50 Ω	Z_T=100 Ω	Z_T=150 Ω	Z_T=200 Ω
Length L_B (m)	497.52	476.77	456.56	438.71	422.68
Current I_A (A)	0.1071	0.1006	0.0943	0.0890	0.0844
Potential bias Φ_C (V)	−0.5353	−5.0297	−9.4338	−13.3458	−16.8703

Table 7 The length L_B in different cases

$\Phi_{\rm PW}$ (V)	0	10	20	30	40	50
Length L_B (m)	273.96	317.84	362.07	406.72	451.85	497.52

from 5 to 200 Ω with increments of 50 Ω while the value of $\Phi_{\rm PW}$ is fixed at 50 V (see Table 6). As shown in Figure 6, it is observed that the potential bias at the cathodic end Φ_C is significantly affected by the change of electric impedance Z_T. Thus, as shown in Figure 6(a), the variation tendency of the profiles of electrical current along the conductive tether is evident. For example, the potential bias Φ_C changes from −0.5353 to −16.8703 whereas the maximum current I_C decreases from 0.1071 to 0.0844 A. This indicates that the variation of impedance Z_T can significantly affect the electron collection efficiency of the EDT system. Moreover, the phenomenon of significant change of impedance may occur when the additional battery is draining out. Therefore, the effect of changing the impedance Z_T should be considered in the refined mission analysis. Further, $\Phi_{\rm PW}$ varies from 0 to 50 V in increments of 10 V while the impedance Z_T is fixed at 5 Ω (see Table 7), and the results are shown in Figure 7. It can be observed that the variation of $\Phi_{\rm PW}$ has a huge impact on the electron collection efficiency of the EDT system. For example, the length L_B decreases from 497.52 to 273.96 m, which indicates that the electron collection efficiency of the EDT decreases by 45%. Therefore, we can conclude that the variation of Z_T and $\Phi_{\rm PW}$ has a significant impact on the electron collection efficiency of an EDT system. Furthermore, the draining out of the additional battery may occur in the demonstration mission, as shown in Figure 2. Therefore, the battery drain out affecting the electrical current should be considered in the mission analysis.

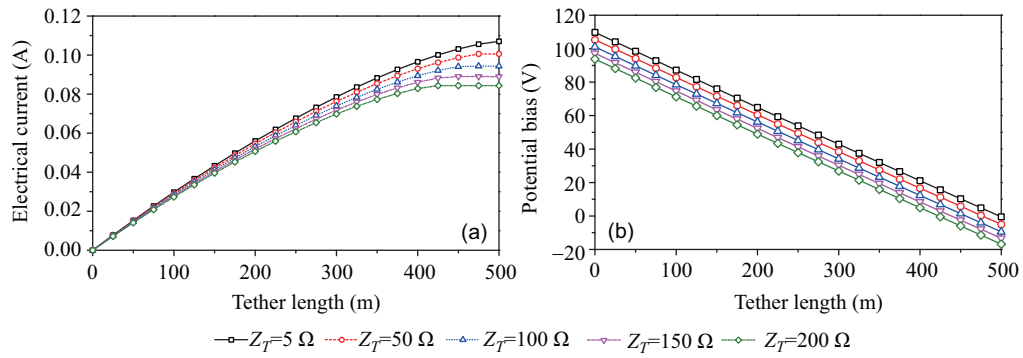

Figure 6 (Color online) Analysis of the impedance Z_T. (a) Electrical current profile along tether; (b) potential bias profile along tether.

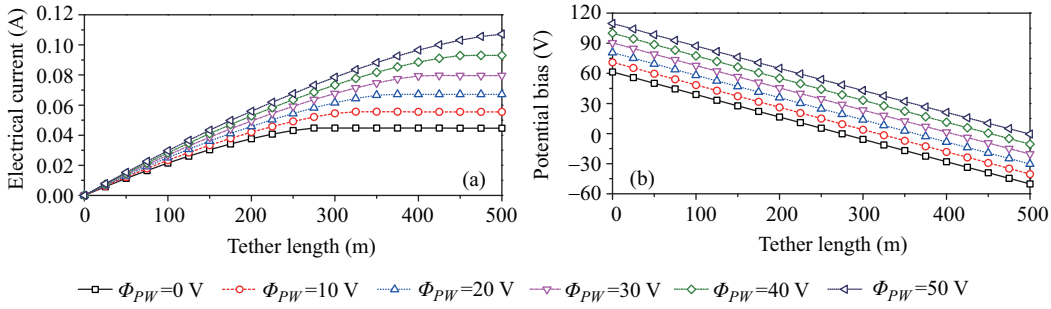

Figure 7 (Color online) The analysis of the potential bias of battery $\Phi_{\rm PW}$. (a) Electrical current profile along tether; (b) potential bias profile along tether.

4 Conclusion

This work develops a fully coupled multiphysics finite element method for the dynamic analysis of an electrodynamic tether system. In the proposed approach, the OML equations are directly discretized by the nodal finite element method in space, and synchronously solved together with the tether dynamics by using the same mesh. The effects of the number of elements, tether bending profile, orbital inclination angle, and design parameters Z_T and $\Phi_{\rm PW}$ at the cathodic end affecting the electrical current have been investigated. The results of parameter analysis demonstrate that the flexible tether geometry and the parameters Z_T and $\Phi_{\rm PW}$ at the cathodic end have a significant impact on the electron collection efficiency of a bare EDT system. These effects should be considered in the refined mission analysis.

Acknowledgements This work was supported by Discovery Grant and Discovery Accelerate Supplement Grant of Natural Sciences and Engineering Research Council of Canada.

References

1 Shan M, Guo J, Gill E. Review and comparison of active space debris capturing and removal methods. Prog Aeosp Sci, 2016, 80: 1–32
2 Macdonald M, McInnes C, Bewick C, et al. Concept-of-operations disposal analysis of spacecraft by gossamer structure. J Spacecr Rockets, 2015, 52: 517–525
3 Sanmartin J R, Lorenzini E C, Martinez-Sanchez M. Electrodynamic tether applications and constraints. J Spacecr Rockets, 2010, 47: 442–456
4 Yu B, Wen H, Jin D, et al. Theory and experiment of space electrodynamic tether systems. Adv Mech, 2016, 46: 226–266
5 Takeichi N. Practical operation strategy for deorbit of an electrodynamic tethered system. J Spacecr Rockets, 2006, 43: 1283–1288
6 Wen H, Jin D, Hu H. Three-dimensional deployment of electro-dynamic tether via tension and current control with

constraints. Acta Astronaut, 2016, 129: 253–259
7 Zhang J, Zhu Z H, Sun Z W. Reduction of libration angle in electrodynamic tether deployment by Lorentz force. J Guid Control Dyn, 2016, 40: 164–169
8 Kawamoto S, Makida T, Sasaki F, et al. Precise numerical simulations of electrodynamic tethers for an active debris removal system. Acta Astronaut, 2006, 59: 139–148
9 Li G, Zhu Z H, Meguid S A. Libration and transverse dynamic stability control of flexible bare electrodynamic tether systems in satellite deorbit. Aerosp Sci Technol, 2016, 49: 112–129
10 Wen H, Zhu Z H, Jin D, et al. Model predictive control with output feedback for a deorbiting electrodynamic eTther system. J Guid Control Dyn, 2016, 39: 2455–2460
11 Li G, Zhu Z H, Ruel S, et al. Multiphysics elastodynamic finite element analysis of space debris deorbit stability and efficiency by electrodynamic tethers. Acta Astronaut, 2017, 137: 320–333
12 Li G, Zhu Z H. Multiphysics finite element modeling of current gneration of bare flexible electrodynamic tether. J Propul Power, 2017, 33: 408–419
13 Pelaez J, Sanjurjo M. Generator regime of self-balanced electrodynamic bare tethers. J Spacecr Rockets, 2006, 43: 1359–1369
14 Sanjurjo-Rivo M, Sáchez-Arriaga G, Peláz J. Efficient computation of current collection in bare electrodynamic tethers in and beyond OML regime. J Aerosp Eng, 2015, 28: 04014144–04014151
15 Sáchez-Arriaga G, Bombardelli C, Chen X. Impact of nonideal effects on bare electrodynamic tether performance. J Propul Power, 2015, 31: 951–955
16 Lanoix E L M, Misra A K, Modi V J, et al. Effect of electromagnetic forces on the orbital dynamics of tethered satellites. J Guid Control Dyn, 2005, 28: 1309–1315
17 Rocchi A, Lavagna M. Versatile electro-dynamic tethers dynamics simulator for debris mitigation tools design. In: Proceedings of the 13th Symposium on Advanced Space Technologies in Robotics and Automation, Noordwijk, 2015. 96077–96085
18 Zanutto D, Lorenzini E C, Mantellato R, et al. Orbital debris mitigation through deorbiting with passive electrodynamic drag. In: Proceedings of the 63th International Astronautical Congress, Naples, 2012. 1–9
19 Zhong R, Zhu Z H. Long-term libration dynamics and stability analysis of electrodynamic tethers in spacecraft deorbit. J Aerosp Eng, 2014, 27: 04014020–04014033
20 Li G, Zhu Z H, Cain J, et al. Libration control of bare electrodynamic tethers considering elastic-thermal-electrical coupling. J Guid Control Dyn, 2016, 39: 642–654
21 Li G Q, Zhu Z H. Precise analysis of deorbiting by electrodynamic tethers using coupled multiphysics finite elements. J Guid Control Dyn, 2017
22 Wang C, Li G, Zhu Z H, et al. Mass ratio of electrodynamic tether to spacecraft on deorbit stability and efficiency. J Guid Control Dyn, 2016, 39: 2192–2198
23 Sun F, Zhu Z, LaRosa M. Dynamic modeling of cable towed body using nodal position finite element method. Ocean Eng, 2011, 38: 529–540
24 Li G Q, Zhu Z H. Long-term dynamic modeling of tethered spacecraft using nodal position finite element method and symplectic integration. Celest Mech Dyn Astr, 2015, 123: 363–386
25 Sanmartin J, Martinez-Sanchez M, Ahedo E. Bare wire anodes for electrodynamic tethers. J Propul Power, 1993, 9: 353–360
26 Zhu Z H. Dynamic modeling of cable system using a new nodal position finite element method. Int J Numer Meth Biomed Eng, 2010, 26: 692–704
27 Zhu Z H. Mission design for a cubesat deorbit experiment using an electrodynamic tether. In: Proceedings of AIAA/AAS Astrodynamics Specialist Conference, Long Beach, 2016. 5573–5579